

# 6 Morphological Instabilities in Flows with Cooling, Freezing or Dissolution

J. A. Whitehead<sup>1</sup> and R. W. Griffiths<sup>2</sup>

<sup>1</sup> Woods Hole Oceanographic Institution, Woods Hole, MA 02543, USA

<sup>2</sup> Research School of Earth Sciences, The Australian National University, Canberra 0200 ACT, Australia

## 6.1 Introduction

The Earth's crust is shaped by a wide range of fluid flows and their characteristic instabilities. Here we consider the flow of silicate melts, either within the crust or as surface lava flows, and the way in which these flows are affected by variable viscosity due to cooling or by a yield strength resulting from solidification. These effects invariably lead to non-uniform or three-dimensional flow patterns, particularly fingering and channelisation. In the case of solidifying free-surface flows there is, in addition, a range of three-dimensional surface structures or deformation styles depending on flow conditions. Parallels can be drawn with channeling instabilities that occur in either the dissolution of a porous matrix or precipitation reactions within a matrix during the percolation of an interstitial fluid.

The flow of magma through the upper-most solid mantle and crust is fundamental to the formation and evolution of the crust, which is formed and re-worked through geological time by the rise of melts towards the surface. The melts, whether granitic or basaltic, do not ascend in a uniform and steady fashion but are instead influenced by heat loss to the relatively cool surrounding rock and consequent variation in viscosity. They rise through channels or, in some cases, as diapirs. The channels, at least sills and dykes in the upper crust, where temperature differences are larger, tend also to evolve from two-dimensional slots to more focused three-dimensional channels [6,24]. Thus volcanic eruptions tend to occur not through a uniform percolation of melt, nor through uniform two-dimensional flow from a dyke, but from localised vents. We therefore begin with a discussion of the fingering instability that causes the flow of cooling melts in two-dimensional sills or dykes to become focused into three-dimensional channels. We then turn in Sect. 6.3 to the case of channelling of the flow of aqueous solution through a soluble porous medium.

Much of the Earth's surface, indeed much of the mass of the planet's crust, was at some time laid down by lava flows, whether submarine (from mid-ocean ridges, seamounts or plume-related volcanic hotspots) or sub-aerial (from volcanism above subduction arcs or hotspots) (see Chap. 5). Hence we devote some of this article to simple models of lava flows and the instabilities that shape them, noting two factors in particular. First, that lava is not a simple Newtonian liquid but is generally a mix of silicate liquid, crystals and gas bubbles

with complicated rheology that may vary from close to Newtonian in the case of the hotter basaltic eruptions (e.g. Hawaiian channel flows) to a rheology having a large yield strength in the case of the high crystal content andesitic lavas of arc volcanoes (such as those of Japan and Indonesia). Second, that surface heat fluxes from the lava flows are generally large enough to cause rapid quenching of a thin surface layer [22], whereas the slower process of crystallization leads eventually to complete solidification of the flow. The behaviour of lava flows, their structure, rate of flow front advance and instabilities varies according to the properties of the erupted magma, the effusion rate, the ground topography over which it flows and the rate of heat loss (determined primarily by the environment) [22,42,47]. The flow front eventually comes to a halt as a result of cooling or ground topography.

In Sect. 6.4 we analyse the spreading of a high yield strength material under gravity as a free-surface gravity current on a sloping plane, but ignoring effects of cooling. In Sect. 6.5 we discuss dimensional analysis and laboratory experiments with cooling and freezing gravity currents on a horizontal base which demonstrate many of the instabilities and morphological characteristics of real flows. These show some similarities with the fingering instability due to viscosity increase of Sect. 6.1, but are substantially different in that the cooling is confined to a very thin surface boundary layer and in that a wider range of behaviour is observed. We then turn in Sect. 6.6 to a discussion of experiments with freezing flows on a slope. A more extensive review of work on cooling and solidifying free-surface flows can be found in [22].

## 6.2 Viscous Fingering Instabilities

It is well-known that the intrusion of a less viscous fluid into a two-dimensional slot (or a porous medium) containing a more viscous fluid leads to inter-fingering of the two fluids as a result of the Saffman–Taylor instability [43]. This is an isothermal phenomenon but relies on the viscosity contrast across the advancing front. A more complex case, but one which is more relevant to the flow of hot silicate melts in the earth’s crust, is that in which the flow involves only one fluid but the viscosity is a function of temperature, so that the dynamics of flow become strongly coupled with the heat flow.

Following [48] we consider a flow in a narrow slot with walls at temperature  $T_W(z)$  and which is fed from below by hotter fluid at temperature  $T_H$  from a two-dimensional chamber as sketched in Fig. 6.1.

The bottom of the chamber is fed by an initially uniform volumetric flux  $Q$  propelled by pressure  $P$ . The slot gap width is  $d$ , the depth of the slot in the  $z$  direction is  $L$  and the slot is infinite in the lateral ( $x$ ) direction. Reynolds number is small, so the flow is governed by a balance between viscous drag and pressure. Following [23,52] the velocity is two dimensional and tangential to the slot walls, so  $\mathbf{u}' = (u', w')$  where  $u'$  is lateral velocity and  $w'$  is out of the chamber. Primes on velocity, pressure, and viscosity denote dimensional quantities. Corrections due to three dimensional variations in temperature and velocity are developed in

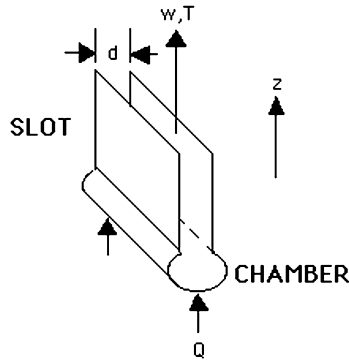


**Fig. 6.1.** Sketch of the idealized system for finger instability. Fluid comes in at the bottom of a chamber. It flows through a slot whose sidewalls are cooler than the fluid

[51], but here we make a simple narrow gap approximation. If the dimensionless number  $\alpha = g\rho\alpha'(T_H - T_W)L/P$  is small, where  $\rho$  is density in the chamber and  $\alpha'$  is coefficient of thermal expansion, effects of gravity  $g$  are negligible [23]. The basic equations are

$$\frac{12\mu'(T)}{d^2}\mathbf{u}' = -\nabla p', \quad (6.1)$$

$$\nabla \cdot \mathbf{u}' = 0, \quad (6.2)$$

and

$$\frac{\partial T}{\partial t} + \mathbf{u}' \cdot \nabla T = -\frac{\pi^2\kappa}{d^2}T. \quad (6.3)$$

Following [23], we investigate two-dimensional flow in the slot. We use a model where the temperature of the walls is uniform and viscosity obeys the law  $\mu' = \mu_H \exp[\lambda'(T_H - T)]$ , which in nondimensional form is  $\mu = \exp[\lambda(1 - \theta)]$  where  $\mu_H$  and  $\lambda'$  are constants. This introduces the dimensionless quantities  $\mu = \mu'/\mu_H$  and  $\theta = (T - T_W)/(T_H - T_W)$ , and the dimensionless number  $\lambda = \lambda'(T_H - T_W)$ . In the scaling we also use  $L$  for a length scale,  $L/U$  for a time scale, and  $U = Pd^2/12L\mu_H$  for a velocity scale. The dimensionless streamfunction defined by  $(u, w) = (-\psi_z, \psi_x)$  (primes are dropped for dimensionless flow variables) obeys the scaled vorticity equation

$$\nabla^2\psi = -\frac{d\ln\mu}{d\theta}\nabla\psi \cdot \nabla\theta. \quad (6.4)$$

In the heat equation we neglect lateral conduction of heat in the plane of the slot compared to conduction from the fluid to the walls, leaving

$$\frac{\partial\theta}{\partial t} + J(\psi, \theta) = -\delta\theta. \quad (6.5)$$

Here, the second dimensionless number in the problem is  $\delta = 12\pi^2\kappa\mu_H L^2/Pd^4$ . This is the inverse of a modified Peclet number  $Ud^2/\kappa L$  [48]. Physically,  $\delta$  is the ratio of the time that it takes for hot fluid to traverse the slot length divided by the time scale for the fluid temperature to respond to changes in wall temperature. Typically, the usual Peclet number  $Pe = UL/\kappa$  will be quite large. For example, for a fissure with  $U = 1 \text{ m s}^{-1}$ ,  $l = 10^3 \text{ m}$  and  $\kappa = 10^6 \text{ m}^2 \text{ s}^{-1}$ ,  $Pe = 10^9$ . However, the ratio  $d^2/L^2$  is typically small and may span wide ranges from  $10^{-6}$  to  $10^{-12}$ , reflecting a variation in expected dike widths from  $10^{-3} \text{ m}$  to  $1 \text{ m}$ . Thus the modified Peclet number  $\delta$  can span a wide range of values both greater and less than one. The dynamic boundary condition at the flow exit is  $u = -\partial\psi/\partial z = 0$  at  $z = 1$ . At the entrance, the condition is  $\theta = 1$ .

The basic steady-state temperature and viscosity fields are readily found as a function of imposed flow  $w_0$  and correspond to a multi-valued pressure drop for  $\lambda > 3.03$  (as shown in Fig. 6.2). Inspection shows that for sufficiently large  $\lambda$  there are values of  $w_0$  that lead to a decreasing magnitude of the pressure gradient for increasing  $w_0$ . This happens because viscosity is small for the warmer temperatures at higher flow rates and is larger for the cooler temperatures at slower flow rates. For a balance between pressure gradient and steady flow, the only recourse is for uniform flow to break down to spatially uneven flow. The feedback mechanism, whereby a change in flow rate makes an inverse change in flow resistance, is the essential factor that causes instability.

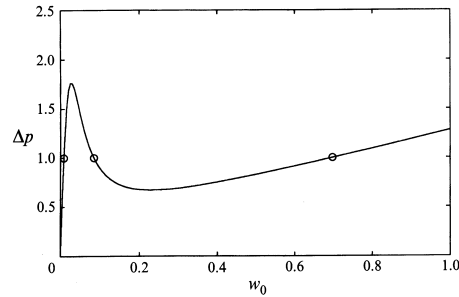


**Fig. 6.2.** Pressure difference across the slot as a function of steady flow rate. In this example  $\lambda = 5$  and  $\delta = 0.1$ . The three circles show that there are three values of flow rate for the same value of pressure difference. At the intermediate circle the flow can be expected to be unstable since a faster flow makes less resistance

A linear stability analysis [23] reveals that, if the basic flow is set in the region where pressure decreases with increasing flow, the flow becomes channelized. The wavelength of most rapid growth is sensitive to the source conditions used (Fig. 6.3). With constant source flux the wavenumber of most rapid growth is of order one. With uniform source pressure the fastest growth is found for zero wavenumber.

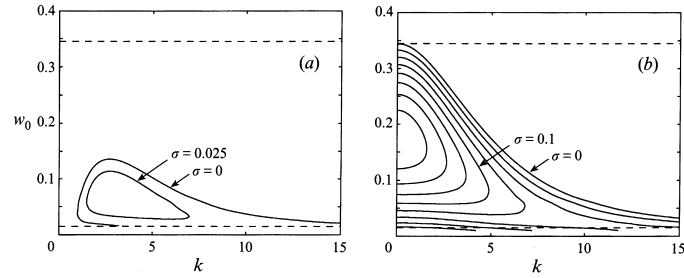


**Fig. 6.3.** Growth rate as a function of wavenumber for two boundary conditions with  $\lambda = 5$ . The values of  $w_0$  are varied rather than  $\lambda$  because the latter is not single valued. On the left a constant source flux is imposed into the slot and on the right a constant pressure is imposed

Numerical studies of the evolution of the temperature and streamfunction field (Fig. 6.4) illustrate the formation of fingers, which represent channels of enhanced flow. Similar channels have been viewed in syrup flowing between two walls with one wall highly cooled [52].

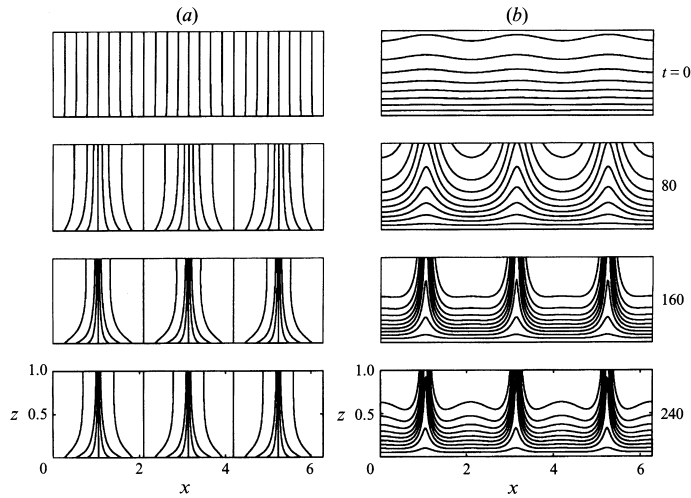


**Fig. 6.4.** Isotherms (*right*) and streamfunction (*left*) at different times for the finger instability. In this case  $\lambda = 5$ , and  $w_0 = 0.0425$  ( $\delta = 0.075$ ). The initial condition was the linear solution for fastest growth

Experiments with liquid paraffin, and described in the following paragraphs, demonstrate the transition from uniform flow to fingering flow as time progresses. The apparatus consisted of a thick square aluminum plate placed horizontally

and levelled carefully in a pan of ice water. Only the underside of the plate was in contact with the water. The temperature of the ice water was estimated to be approximately  $5^\circ\text{C}$  in contact with the plate, since the ice floated only around the edges of the plate. A 11 mm thick square plexiglas plate 4.6 mm on a side was clamped over the aluminum with spacers between the aluminum and plexiglas leaving a narrow gap of  $2.4 \pm 0.7$  mm. A hole drilled in the center of the plexiglas was connected by a heated hose to a reservoir containing melted paraffin. As a run commenced, paraffin was delivered to the hole at a known constant rate (5.5 ml/s) by gravity feed. The paraffin initially began to spread out in a growing pattern that was close to perfectly circular. After 16 seconds there was a rapid growth of radial finger-like bulges (Fig. 6.5a) with round tips. Ten or twelve fingers grew within four seconds but many of them stopped growing during the next four seconds. The only change in the pattern subsequently was that four fingers reached the edge of the tank, the rest froze. At this stage oil soluble dye was injected into the paraffin source and it was observed that most flux was into the two largest fingers. Forty eight seconds later the flow was through only one finger (Fig. 6.5b), fed by a single channel, in a flow pattern that then continued indefinitely, with little apparent change.

Assuming that both the lid and the aluminum plate cool the paraffin as it flows along the slot, the thermal time constant for the initial paraffin flow in the gap is of order  $h^2/4\kappa = 14.5$  s ( $\kappa = 0.001\text{ cm}^2\text{ s}^{-1}$ ), which is similar to the observed time to instability of 16 seconds. Furthermore, the final channel (of width approximately 1.5 cm) carried the full source flux from the source to the edge of the plate at a relatively large velocity of around  $15\text{ cm s}^{-1}$ . Hence the fluid at this stage spent less than 2 s in the slot, a time that is short compared to



**Fig. 6.5.** The evolution of paraffin flowing with constant volume flux through a cooled annular slot from a small source. (a) Numerous fingers have broken out at 20 seconds from an intrusion that was circular at a time of 12 seconds. (b) At 92 seconds dark dye reveals that the fingers have all stopped except for one channel. The red dye was placed in the fluid earlier and it indicates a previous time when there were two channels. Extended fingers also reveal that there was a time with four channel flow

the time required for it to cool. In this manner the fluid adopted both a long and a short length scale for the final flow. The long distance between the remaining active channels led to faster and hence warmer flows in the remaining channels. At the same time each channel became narrow enough to continue to support rapid flow. Thus large channel spacing combined with narrow channels allowed transit of fluid parcels without them becoming too cold.

Our aim here was to demonstrate the simple concept that the system establishes, through instability, a flow pattern that allows fluid to escape from the slot before it cools enough to greatly increase its viscosity. It was found that instability occurred on the time scale for diffusion of heat through the width of the slot, and it took on a large length scale. These results are probably relevant to the flow of magma through conduits in the Earth's crust [6]. Later in this chapter we will see that free-surface gravity currents too, such as lava flows, are unstable due to cooling, but that instability occurs on a very much shorter time scale during which only a very thin superficial boundary layer is cooled and solidified. Again, under some conditions, long narrow channels containing high flow velocity are formed.

### 6.3 Dissolution Instability and Channelised Flow in Permeable Media

A related problem, which in addition involves latent heat effects, is the melting of a permeable matrix (or freezing of melt) during percolation in a porous medium. We consider, as an example, the particular case of a liquid flowing uniformly through a porous material where it encounters a material of lower permeability which it can partially dissolve, and assume the flow is at a constant temperature. Dissolution increases the permeability of the solid matrix. A similar fingering instability that again leads, at finite amplitude, to the channelisation of flow occurs in the percolation of a solvent, such as a hot hydrothermal solution, through a partially soluble permeable matrix.

Following [32], the system to be analysed is sketched in Fig. 6.6.

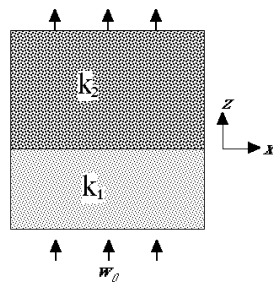


**Fig. 6.6.** Sketch of the initial state for the model of liquid flowing upward through a porous material which it can dissolve

Let the interface lie at

$$\eta(x, t) = z, \quad (6.6)$$

and the equation for the dissolution of the interface be

$$\frac{\partial \eta(x, t)}{\partial t} = \gamma w. \quad (6.7)$$

In this model, dissolution causes the interface to migrate at a rate proportional to the amount of fluid flowing through the interface. We assume that dissolution at the interface immediately increases the permeability from the initial value above the interface to the higher permeability of the material below the initial position of the interface.

For small times we let the total vertical Darcy velocity at the interface  $w$  consist of a steady uniform component plus a small perturbation, and describe the interface as a horizontal plane plus a small deviation:

$$w = w_0 + w'(x, t), \quad (6.8)$$

$$\eta = \eta_0(t) + \eta'(x, t). \quad (6.9)$$

The steady flow and the mean interface position are given by:

$$\frac{\partial \eta_0}{\partial t} = \gamma w_0, \quad (6.10)$$

$$\eta_0 = \gamma w_0 t = z, \quad (6.11)$$

whereas equations governing the perturbations throughout the porous materials are given by Darcy's law:

$$\frac{k_n}{\mu} \frac{\partial p_n}{\partial x} = -u_n, \quad (6.12)$$

$$\frac{k_n}{\mu} \frac{\partial p_n}{\partial z} = -w_n, \quad (6.13)$$

with velocity components

$$u_n = \frac{\partial \psi_n}{\partial z}, \quad (6.14)$$

$$w_n = -\frac{\partial \psi_n}{\partial x}, \quad (6.15)$$

where the streamfunctions  $\psi_n$  satisfy

$$\nabla^2 \psi_n = 0. \quad (6.16)$$

Here,  $\mu$  is the dynamic viscosity,  $k_n$  is the matrix permeability and subscripts  $n = 1, 2$  denote the region upstream or downstream of the interface.

For a perturbation to the interface of the form

$$\eta' = N(t) \cos(lx) \quad (6.17)$$

and, assuming firstly, that  $w_0 \gg w'_n$ , secondly, that we start with  $t = 0$  so the unperturbed interface is at  $z = 0$ , and thirdly that  $N(t)$  is smaller than the length scale  $l^{-1}$ , we integrate (6.13) for  $w$  upward from a plane normal to the bottom of the perturbed interface at  $z = -N$  to a plane normal to the top of the perturbed interface  $z = N$ :

$$\begin{aligned} p_2(N) - p_1(-N) &= -\frac{\mu}{k_2} \int_{\eta'}^N w_0 dz - \frac{\mu}{k_1} \int_{-N}^{\eta'} w_0 dz \\ &= -\mu w_0 \left\{ N \left[ \frac{1}{k_2} + \frac{1}{k_1} \right] + N \cos(lx) \left[ \frac{1}{k_1} - \frac{1}{k_2} \right] \right\}. \end{aligned} \quad (6.18)$$

A contribution to the above calculation for pressure from perturbation velocity  $w'$  is of order  $w'N$  and is assumed to be negligible. Equation (6.18) divided by  $2N$  is the average vertical pressure drop in this region. Of primary interest is the laterally varying component of pressure, which by symmetry, we take to be zero at the origin, so that

$$\left. \frac{\partial p_2}{\partial x} \right|_N = - \left. \frac{\partial p_1}{\partial x} \right|_{-N} \quad (6.19)$$

and laterally varying pressure at  $z = N$  is

$$\frac{\partial p_2}{\partial x} = \frac{\mu w_0 N l}{2} \left[ \frac{1}{k_1} - \frac{1}{k_2} \right] \sin(lx). \quad (6.20)$$

Since  $N$  is indefinitely small, this condition will be assumed to apply at  $z = 0$ .

Using (6.12) and the streamfunction definition

$$u_2 = \frac{\partial \psi_2}{\partial z} = -\frac{k_2}{\mu} \frac{\partial p_2}{\partial x} = -\frac{w_0 N l k_2}{2} \left[ \frac{1}{k_1} - \frac{1}{k_2} \right] \sin(lx). \quad (6.21)$$

A solution to (6.16) is

$$\psi_2 = A(t) \sin(lx) e^{-lz}, \quad (6.22)$$

which with (6.21) at  $z = 0$  produces

$$A(t) = k_2 w_0 \left[ \frac{1}{k_1} - \frac{1}{k_2} \right] N(t). \quad (6.23)$$

Using (6.7), (6.8), (6.10), (6.15), (6.17), and (6.23) results in

$$\frac{\partial N}{\partial t} = -\gamma l w_0 \left[ \frac{k_2}{k_1} - 1 \right] N, \quad (6.24)$$

which has an exponentially growing solution for  $k_1 > k_2$  (upstream permeability greater than downstream). Equation (6.24) shows that the larger the wavenumber  $l$  the faster the growth rate. Therefore, very small length scale perturbations grow most rapidly.

The stability of an initially planar interface and the subsequent spatial distributions of permeability, porosity, solute concentration and water composition were studied by Ortoleva et al. [38,39]. They found that the planar interface is unstable with the fastest growing wavelength determined by matrix size, initial modal amount of reactive mineral in the rock, initial porosity, the composition and the velocity of the inlet fluid. In essence their result simplifies to the wavelength of fastest growth being proportional to thickness of the front, which is determined by the effective solute diffusivity divided by the fluid Darcy velocity. Since the effective diffusivity (due to mechanical dispersion) of a solute flowing through a porous material is proportional to the Darcy velocity times grain size, this reduces to the simple result that finger width is proportional to grain size. The purpose here was to present the essentials of such an instability in as simple form as possible. Hence many of the elements included in the original analysis, such as grain size, porosity variation, and change in volume of the solute, were neglected.

The more complete theories of Ortoleva et al. [38,39] have shown that diffusion processes limit the magnitude of the fastest growing wavenumber, so that fastest growth is scaled by grain size. The first wavelengths to appear in experiments with water percolating through salt agree with this [38]. They are small but larger than grain size, which contrasts with the very long wavelength favored in the viscous fingering case of Sect. 6.2. For longer times the short wavelength distortions attained a finite size and stopped their exponential growth, while longer wavelengths continued to grow. Flows produce drainage channels that exhibit both coalescence and branching [32,49].

Finger instability may also be encountered in reaction–dissolution effects upon the migration of melt. In order to describe the migration of melts to produce magmas it is necessary to add the process of compaction (the driving of the fluid by gravity acting on a viscous deformable solid matrix of different density). For example, mid-ocean ridge basalts (MORB) are produced through pressure-dependent melting (the melting temperature decreases with decreasing pressure) coupled with compaction-driven flow. Melt accumulates around grain boundaries and is squeezed upwards by the slowly deforming denser mantle crystals. The composition of the mantle is such that rising mantle material undergoes partial melting as it reaches lower pressures. Hence melt percolating upward will be out of chemical equilibrium with the remaining matrix of mantle crystals and will produce additional reaction that in general will reduce the permeability. In the absence of compaction [1], the porous flow of a reacting fluid through a soluble matrix with gradually changing solubility has growing finger instabilities over the entire range of Damkohler numbers  $Da = l/L_{eq}$ . Here  $L_{eq} = \phi_0 w_0 \rho_f / R_{eff}$  is the distance that a perturbation in chemical concentration will travel before becoming chemically equilibrated, and thus it is the product of velocity and reaction time. (In this formula,  $\phi_0$  is the porosity,  $\rho_f$  is density of the melt,  $R_{eff}$  is the reaction rate of the melt in contact with a crystal matrix, and the other symbols are as above.) However, in a compacting matrix not all reacting flows are unstable [1]. The criterion for instability is that  $Da > 1/Cn$ , where  $Cn$

measures the effects of the change in solubility over one compaction length  $h_{comp}$  multiplied by the ratio of compaction length to matrix depth. A compaction length is the distance a change in matrix porosity can migrate in a compacting flow before decaying. The stability criterion is also written as  $\beta' h_{comp}^2 / L_{eq} > 1$ , where  $\beta' h_{comp}$  is the change in solubility over one compaction length.

Finite amplitude effects of instability have been observed in laboratory studies without matrix compaction [32,49] and also in a number of computer studies [2,33,45]. In numerical studies the channels that break out as the result of instability typically branch and coalesce again. Branching is also seen in the related problem of Saffman–Taylor instability and may be simply a function of the degree to which the stability criterion is exceeded. However, the thermal channels in cooled laboratory viscous flows observed to date do not exhibit such branching, and the exact causes of channel branching and coalescence are poorly understood.

#### 6.4 The Shapes of Free-surface Yield-strength Flows on a Slope

Some lava flows, especially those having relatively high silica content, tend to be erupted with high crystal and vesicle fractions that give them a highly non-Newtonian rheology. This rheology is most simply characterised by the addition of a large yield stress to the viscous stress in the stress-strain rate relation. Therefore, a very useful (but highly simplified) flow to understand is the isothermal flow of a yield-strength material as it is slowly extruded onto a sloping plane from a localised source (or vent). This is the next step beyond an analysis of the radial spreading of a viscoplastic fluid from a source on a horizontal plane [3,5], where the flow is characterised (apart from significant viscous stresses in a small neighbourhood of the source) by a static, or quasi-equilibrium, balance between gravity and yield strength at any distance from the axial source. A simple parabolic height profile with radius results, and the dome remains axisymmetric as it expands over the horizontal base, apart from a set of orthogonal spiral glide planes on which the material achieves the deformation that is necessary for it to spread radially.

Early realisation that the levee banks created by long basalt flows implied non-Newtonian flow led Hulme [26] to consider the unconfined motion of a Bingham fluid of yield stress  $\sigma_0$  down a slope. He considered long flows and assumed that all quantities are independent of distance  $x$  down-slope. Near the edges of a flow its depth  $h(y)$  becomes small and the lateral flow was assumed to cease when the cross-slope pressure gradient is balanced by the basal yield stress, as expressed in

$$\frac{\partial P}{\partial y} = \rho g \frac{\partial h}{\partial y} = \frac{\sigma_0}{h}. \quad (6.25)$$

This model is based on the assumption that the fluid does not deform anywhere but at its base, where the pressure is greatest and (in order for the fluid to have reached its current shape) equal to the yield stress. The solution to

(6.25), originally obtained in the context of icesheet dynamics [37], with  $h = 0$  at  $y = W$ , is simply

$$h^2 = \frac{2\sigma_0}{\rho g} (W - y) , \quad (6.26)$$

which implies that the central height  $H = h(0)$  and the half-width  $W$  are always related by  $H = C(\sigma_0 W / \rho g)^{1/2}$ , where  $C = \sqrt{2}$ . If the flow depth is assumed to be constant in the down-slope direction at any value of  $y$ , then motion requires  $\rho g h(y) \sin \beta > \sigma_0$ , where  $\beta$  is the slope of the base from the horizontal. Hence there is a critical depth

$$h_s = \frac{\sigma_0}{\rho g \sin \beta} \quad (6.27)$$

below which there will be no down-slope motion. Substituting this depth into the cross-slope balance (6.26) gives the width of the region of stationary fluid along the edge of the flow:

$$w_s = \frac{\sigma_0}{2\rho g \sin^2 \beta} = \frac{h_s}{2 \sin \beta}. \quad (6.28)$$

Between these two stationary regions there is free visco-plastic flow down-slope, which Hulme approximated as the two-dimensional flow between a parallel stress-free surface and no-slip bottom plane, leading to the depth-averaged velocity [26,44]:

$$u = \frac{\rho g \sin \beta h_s^2}{3\eta} \left[ \left( \frac{h}{h_s} \right)^3 - \frac{3}{2} \left( \frac{h}{h_s} \right)^2 + \frac{1}{2} \right]. \quad (6.29)$$

An error in Hulme's analysis is that, for the cross-slope motion to cease, it is necessary to consider more than the cross-slope component alone of the basal stress: the total stress  $\sigma = \rho g h [\sin^2 \beta + (\partial h / \partial y)^2]^{1/2}$  at the base (where the down-slope thickness gradient might be neglected) must become equal to the yield stress.

Laboratory experiments with kaolin-water slurry on a slope [26] revealed the presence of stationary levees bounding long down-slope flows. The height of the levees was consistent with the formula (6.27), which was then applied to lava flows to find yield strengths for various flows (of order  $10^3$  Pa for low silica contents to  $10^5$  Pa for higher silica contents) from the height of levees (5–30 m) and the underlying topographic slope. This much of the behaviour of long flows, and particularly the observed levees, can therefore be explained in terms of isothermal flows having a yield strength. The levee-derived correlation between silica content and strength for terrestrial flows, along with remote measurements of levee heights, were even used to estimate compositions of lunar flows. In detail, real flow levees are formed of cooled flow-front or surface material pushed aside by the advancing flow front, so that only the levees are required to have a yield strength and the flow is not of uniform rheology. However, the principle and the application of (6.27) are unchanged.

A more difficult problem is posed by domes of extremely 'stiff', high-silica content, lavas erupted on to slopes; these are not the very long flows (or relatively

low-viscosity basalt) which motivated the previous work [21,22]. Instead, the challenge is to predict the fully three-dimensional shapes, including the extent of up-slope flow from the vent. A solution for the analogous problem of Newtonian viscous flows was given by Lister [35]. The solution can also be found for the three-dimensional case in the limit of slow flow or high yield strength (i.e. when  $B \rightarrow \infty$ , where  $B = \sigma_0/\eta\dot{\epsilon} = \sigma_0 h_s/\mu U$ , with  $U$  a velocity scale and  $\mu$  the viscosity, is the Bingham number comparing yield stress to viscous stresses). In this case, the extruded material causes a force that exceeds the yield stress. This produces a flow that terminates as a new balance between yield stress and hydrostatic forces is produced. Elements of this solution were given by Coussot et al. [8,9], who thought the complete solution would be non-unique, but the unique solution for emplacement from a small source was obtained by Osmond & Griffiths [40]. This solution is summarised here and gives the three-dimensional shape for static finite volumes. It also gives the final width of very long down-slope flows (i.e. for large volumes), which turns out to be independent of the viscosity.

We assume  $H/L \ll 1$ , a hydrostatic gradient in the vertical and a static balance between gravity and yield stress (as in (6.25) but this time in the plane parallel with the base slope) and that the total stress at the base is equal to the yield stress. We readily obtain an equation for thickness  $h(x, y)$  normal to the base [40]:

$$\left(\frac{\partial h}{\partial x} - \tan \beta\right)^2 + \left(\frac{\partial h}{\partial y}\right)^2 = \left(\frac{\sigma_0}{\rho g h \cos \alpha}\right)^2. \quad (6.30)$$

The axes  $x$  and  $y$  lie in the plane of the sloping base, the  $z$  axis normal to the base. Assuming symmetry about the down-slope ( $x$ ) axis through the source implies  $[\partial h/\partial y]_{y=0} = 0$  (except at  $x = 0$ , where  $\partial h/\partial y$  must be discontinuous in order to force radial flow from the vent). Then (6.30) can be solved for the thickness profile  $h(x, 0)$ . Scaling thickness  $h$  by  $h_s$  (6.27) and distance  $x$  parallel to the sloping base by  $h_s/\sin \beta$  gives the thickness profiles (with all quantities now dimensionless)

$$\begin{aligned} x &= h - H + \ln |(1-h)/(1-H)|, & x \geq 0, \\ x &= h - H + \ln |(1+h)/(1+H)|, & x \leq 0, \end{aligned} \quad (6.31)$$

on the down-slope ( $x > 0$ ) and up-slope ( $x < 0$ ) sides, where  $h = H$  at  $x = 0$ . The leading edges of the dome are found at  $h = 0$  and from (6.31) we have

$$x_d = -H - \ln |1 - H|, \quad x_u = -H + |1 + H| \quad (6.32)$$

(downslope and up-slope respectively) or a total dimensionless flow length  $L = -\ln |1 - H^2|$ . The cross-slope thickness profile of the dome can be approximated by neglecting  $\partial h/\partial x$  in (6.30) in the region of maximum width (down-slope from  $x = 0$ ). The dimensionless maximum width is given by  $W \approx 2(1 - \sqrt{1 - H^2})$ . It tends to be more useful to describe these flows in terms of their volume  $V$  at any time, where  $V$  is the extruded volume normalised by the volume scale:  $\sigma_0^3/[(\rho g)^3 \sin^5 \beta]$ ; the dome is not much influenced by the topography for  $V \ll 1$

but strongly influenced and displaced somewhat down-slope from the vent for  $V > 1$ . When  $V \gg 1$  (and the thickness  $H$  tends to 1) the down-slope length of the dome tends to infinity. This reflects the fact that the critical thickness  $h_s$  (6.27) is the maximum dome thickness that can be supported on the slope in a static balance; larger thickness would imply a basal region of dynamic viscous flow. For  $V \ll 1$  (i.e.  $H \ll 1$  as a result of small volume, large yield strength, small slope or reduced gravity) the dome is not influenced by the base slope, is close to axisymmetric and (6.31) approaches the quadratic profile (6.26).

In order to obtain the complete locus of the dome perimeter and contour plots of flow thickness as a function of  $H$  (or of  $V$ ) equation (6.30) was solved numerically. Sample solutions are shown in Fig. 6.7 for the flow depth contours at several values of the dimensionless volume. Miyamoto & Sasaki [36] treat a similar problem through numerical simulation.

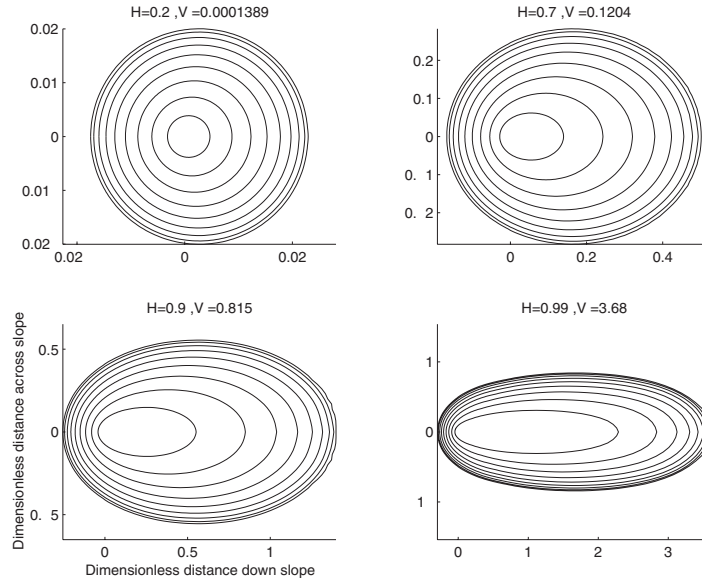


**Fig. 6.7.** Contour plots of flow depth obtained from the numerical solutions (6.30) for yield strength flow on a slope. Solutions are shown for four values of the dimensionless central thickness  $H$  (or dimensionless volume  $V$ ). Note the change in scale on the axes between the various plots. From [40]

The solutions compare well with isothermal experiments with slurries of kaolin in polyethylene glycol wax as well as kaolin in water, both on a sloping base (Fig. 6.8). In experiments with  $V \approx 0.1$  ( $H \approx 0.7$ ), the flow margin begins to depart noticeably from circular and the down-slope length is more than twice the up-slope length from  $x = 0$ . For  $V \approx 1.5$  ( $H \approx 0.95$ ), the down-slope length is eight times greater than the upslope length and nearly twice the full

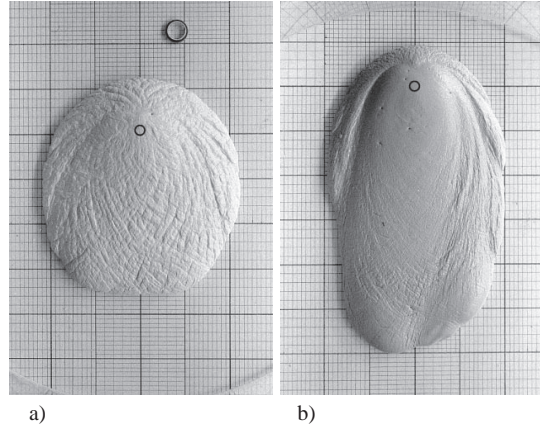


**Fig. 6.8.** Photographs of isothermal laboratory flows of Bingham fluid on a planar slope. The fluid was extruded in many small volume increments from a 1 cm diameter hole in the smooth base. The domes were static between increments. The black circle shows the location of the source. (a) kaolin/water slurry, slope  $\beta = 12^\circ$ , volume  $900 \text{ cm}^3$ ,  $\sigma_0 = 92 \text{ Pa}$ , dimensionless volume  $V \approx 0.8$ ; (b) kaolin/PEG slurry,  $\beta = 18^\circ$ ,  $1000 \text{ cm}^3$ ,  $\sigma_0 = 84 \text{ Pa}$ ,  $V \approx 12$ . ‘Leaves’ develop for  $V > 10$ , when further spreading is largely down-slope. (From [40])

width. Two sets of slip planes again curve out from the summit as in Blake’s [5] experiments on a horizontal base, but this time they are asymmetric in the  $x$ -direction. The stationary levees of Hulme [26] are seen to form along the edges of the down-slope laboratory flow at very large flow elongations ( $V > 10$ ,  $H \rightarrow 1$ ; Fig. 6.8b). In the analysis the assumption of a static balance everywhere implies that the origin is to be identified with the vent from which the fluid was supplied, and there is no implication that fluid volumes having histories different from this will take similar shapes: the static shape will be different if the base slope is changed after the volume is emplaced, or if the flow is rapid and partly viscous for a time before taking on the quasi-static shape controlled by yield strength.

One conclusion to be drawn from these observations is that complex flow structure is not always the result of instability. The levee structures along the edge of the flow form simply because the edges must be shallow and therefore cannot move down-slope in the presence of the yield strength. A down-slope channel is formed, somewhat like those that form in the cooled slot (Sect. 6.2) as a consequence of increased viscosity (or solidification). However, the detailed texture of the surface and the structure of the intersecting yield surfaces have not been addressed. In real lava flows, there are additional complications due to the

effects of cooling and varying rheology, which may greatly alter some flows while leaving others, presumably those emplaced relatively rapidly, less affected.

## 6.5 Instabilities of Solidifying Free-surface Gravity Currents

In the case of the spreading of a fluid on a plane under gravity the flow has a free surface and hence additional freedom to respond to cooling and rheology variation. Isothermal gravity currents, both turbulent and very viscous, have been studied extensively. However, the more complicated (and much richer) problem of cooling gravity currents having temperature-dependent rheology or solidification has barely been touched. Recent work in this area has been motivated by modelling of lava flows, but is also relevant to some industrial problems such as the flow of molten metals.

There are a number of styles and morphologies of lava flow, each presumably reflecting a different dynamical flow regime. Some examples are shown in Fig. 6.9. The style of flow is controlled by factors such as: lava composition and rheology, eruption temperature, effusion rate, base topography and whether it flows under water, air or a vacuum [12]. Initial heat loss is predominantly by radiation under the relatively thin atmospheres of Earth and Mars (Earth's atmosphere has sufficient heat capacity that convection provides a comparable flux only after the surface temperature has fallen to less than  $\approx 200^\circ\text{C}$  [18,22]). In contrast, radiation is less important than convection for temperatures less than  $900^\circ\text{C}$  under the dense atmosphere of Venus (where  $T_a \approx 450^\circ\text{C}$ ). For eruptions under water radiation is always negligible relative to the very rapid convective transport [19].

The effects of cooling will depend on the rate of spreading of the flow relative to the rate of cooling through a temperature range sufficient to cause rheological change. It is therefore logical to first consider the role of a dimensionless parameter expressing this ratio. A comparison of the conductive transport of heat within the lava to the advection of heat with the flow reveals that for almost all lava flows the Peclet number  $Pe = UH/\kappa$  ( $U$  a velocity scale,  $H$  a flow depth scale and  $\kappa$  the thermal diffusivity) is very large, ranging from  $10^2$  to  $10^5$  for slow-growing lava domes through to  $> 10^6$  for fast channelized basalts flows. Thus cooling is confined to a very thin boundary layer at the free surface and, if mixing is absent, the interior remains largely isothermal. In this thin boundary layer regime surface solidification commences at a distance  $d_s \approx ut_s$  from the vent, where  $u$  is the surface velocity and  $t_s$  is the time taken for the surface temperature  $T_c$  to cool from the vent temperature  $T_e$  to the solidification temperature  $T_s$ . Scaling distance by  $H$  and velocity by a suitable scale  $U$  one can define the dimensionless parameter [12,20]

$$\Psi = \frac{Ut_s}{H} = \frac{t_s}{t_A}, \quad (6.33)$$

where  $t_A = H/U$  is the time scale for lateral flow through a distance  $H$ . Equivalently,  $d_s/H \approx \Psi$ . Here the velocity scale  $U$  and the advection timescale  $T_a$  will

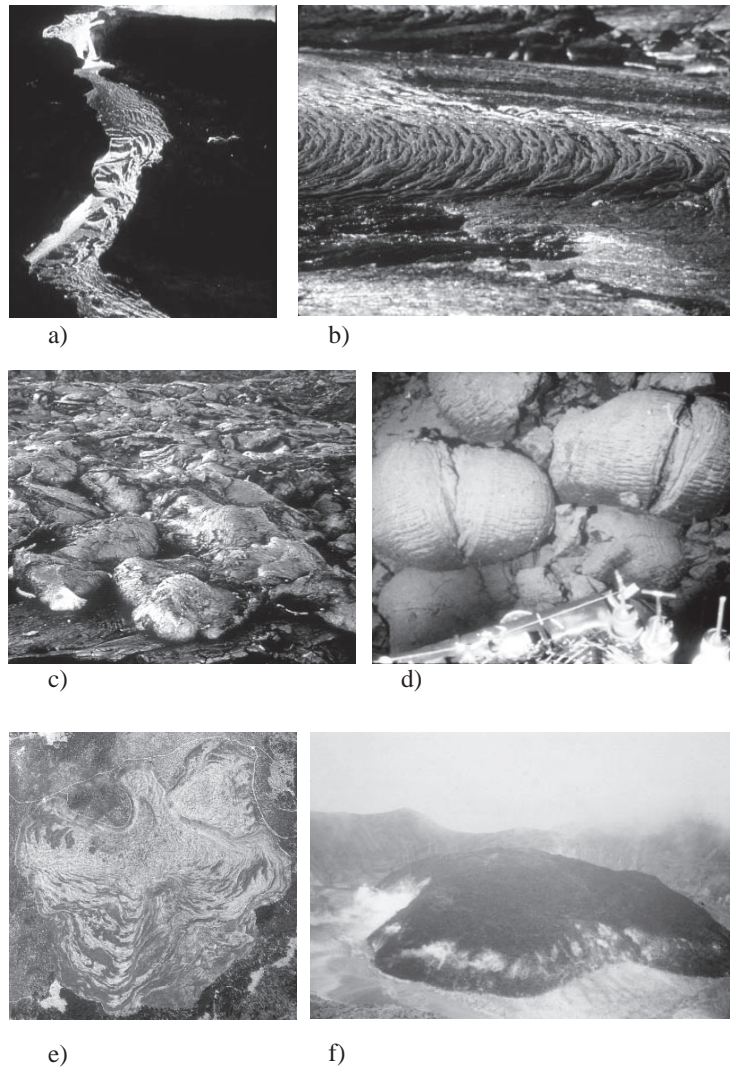


**Fig. 6.9.** Examples of some lava flow forms: (a) channelised basalt flow from Kilauea Volcano, Hawaii (flow channel roughly 20 m wide); (b) and (c) 'ropy pahoehoe' and 'toey pahoehoe', respectively from Kilauea ('ropes' have wavelength  $\approx 20$  cm, 'toes' are typically 30 cm across); (d) submarine pillow basalts, each approximately 1 m across, on the East Pacific Rise; (e) Little Glass Mountain rhyolite flow, northern California, showing flow around an obstacle on a gentle slope and transverse surface ridges  $\approx 5$  m in height (image 2.8 km across); (f) a lava dome 850 m across and 130 m high in the crater of La Soufrière, St Vincent, 1979. Photographs courtesy of J.H. Fink and R. Embley

depend upon the governing dynamics of the flow, as indicated below. The value of  $t_s$  depends on the surface heat flux and the dimensionless temperature of solidification  $\Theta_s = (T_s - T_a)/(T_e - T_a)$ , the proximity of the eruption temperature  $T_e$  to the solidification temperature  $T_s$  [12,20]. This time scale (and the surface temperature  $T_c$ ) must be obtained from a heat transfer calculation, accounting for radiation and convection from the surface [18,19] matched to the conductive heat flux within the lava. The surface solidification time was found to be of the order of 0.1s for submarine lavas, 100s for sub-aerial basaltic lavas (on Earth and Mars), and approximately 60s for the cooler highly-silicic lavas under air. Note that the parameter  $\Psi$  is defined for extrusions of constant volume flux  $Q$  in terms of the advective time scale  $t_A$  appropriate to the corresponding *isothermal* Newtonian gravity currents. A similar parameter  $\Psi_B$  can be defined, again by (6.33), when the flow is plastic [21].

For the Newtonian case (and point source) a global velocity scale  $U = Q/H^2 \approx (\rho g Q/\eta)^{1/2}$  and depth scale  $H = (Q\eta/\rho g)^{1/4}$  are found for the isothermal flow [30] and give  $t_A = (\eta/\rho g)^{3/4} Q^{-1/4}$ , so that the dimensionless solidification time becomes

$$\Psi = \left(\frac{\rho g}{\eta}\right)^{3/4} Q^{1/4} t_s . \quad (6.34)$$

For the plastic case  $U = Q(\rho g/\sigma_0)^2$  and  $H = \sigma_0/\rho g$  [21], and these lead to

$$\Psi_B = \left(\frac{\rho g}{\sigma_0}\right)^3 Q t_s . \quad (6.35)$$

These definitions represent an attempt at describing a flow in a global sense, recognising that the advection velocity at a given radius can vary with time (as the depth changes or the flow becomes non-axisymmetric) and depends on distance from the vent. Thus there remains scope for time-dependence of the effects of solidification within a flow having a fixed value of  $\Psi$ . Of course, variations of source volume flux lead to changes in  $\Psi$  and this is explicit in (6.34, 6.35).

At distances from the vent greater than  $d_s$  the layer of solid crust will thicken in a manner that, again, can be calculated by coupling conduction in the lava to the surface heat flux through the surface temperature  $T_c(t)$  [18,19]. Note that in terms of the external dimensionless parameters,  $\Psi$  and  $\Psi_B$  provide a general indication of whether the solid crust thickens quickly or slowly relative to the lateral motion. These parameters are more relevant to the thickness of the rheological boundary layer than is  $Pe$ , at least at early times, since the latter relates only to the thickness of the thermal boundary layer (given by  $\delta_T \approx (\Psi/Pe^{1/2})H$  at the location of the onset of solidification), and the thermal boundary layer is not directly related to the presence or thickness of crust.

Laboratory analog experiments serve to test the hypothesis that the primary effects of cooling and solidification for slow laminar flows are captured by differences in the parameter  $\Psi$ . The experiments used viscous polyethylene glycol (PEG) wax, which freezes at a convenient temperature of 18–19 °C, extruded from a small circular (or narrow linear) vent under cold water onto a horizontal or sloping base [12,13]. The cold water gave rise to a sufficiently large turbulent

convective heat flux and solidification times comparable to horizontal advection times. The results revealed a sequence of distinct flow regimes (Fig. 6.10) and these correlated with intervals of  $\Psi$  [13].

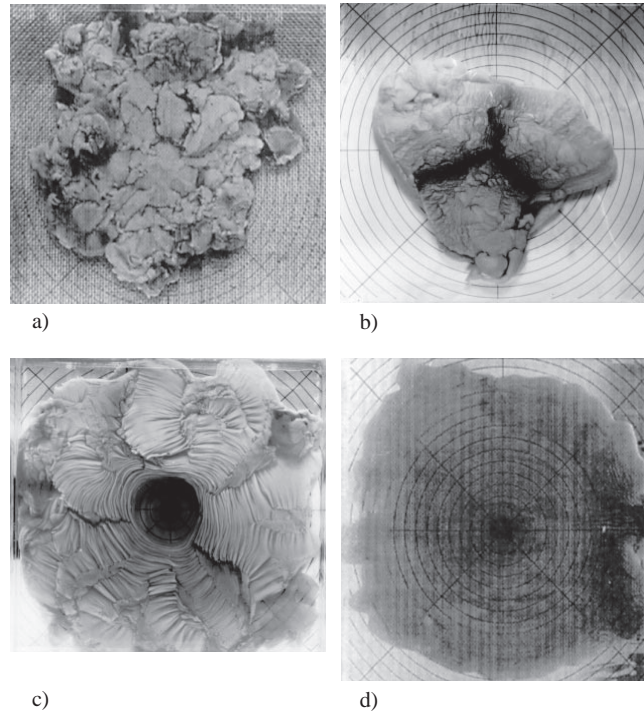


**Fig. 6.10.** Examples of solidifying gravity currents showing four flow types in laboratory experiments with polyethylene glycol wax flowing over a horizontal floor. The Newtonian liquid was extruded from a small hole onto the base of a tank of cold water. Some of the surface subsequently solidified. (a) ‘pillow’ growth at  $\Psi = 0.11$ ; (b) ‘rifting’ flow with separating rigid surface plates at  $\Psi = 2.7$ ; (c) ‘folded’ flow at  $\Psi = 3.0$ ; (d) largely axisymmetric flow with weak cooling and solid confined to ‘levees’ along the flow front at  $\Psi = 7.3$  (these values of  $\Psi$  have been corrected for a previous numerical mistake: all values reported in [12] must be divided by  $10^{2/3}$ )

At  $\Psi < 0.7$ , where cooling is rapid or extrusion is slow, the flow was fully encased in solid and spread through many small bulbous outgrowths reminiscent of submarine lava ‘pillows’; at  $0.7 < \Psi < 2.5$  thick solid extended over most of the surface and formed rigid plates separated by divergent ‘rifts’, complete with transform faults, where solid continued to accrete onto the plates; at  $2.5 < \Psi <$

6 solid became more widely distributed (except over the vent) but was thin and tended to buckle or fold, forming many small transverse ridges and ropy structure; at  $6 < \Psi < 16$  crust was seen only around the margins of the flows, where it formed 'levees'; and at  $\Psi > 16$  no solid crust formed before the flow front reached the side walls of the container (the values of  $\Psi$  given here are smaller, by a factor  $10^{2/3}$ , than those originally reported in [12] because an incorrect value for the water viscosity was originally used). In addition, for  $\Psi < 6$ , the flows ceased to spread when the source flux was turned off, indicating control of spreading by the strength of the solid (i.e. a balance of buoyancy and crust yield strength). The forms of surface deformation and flow morphology observed are similar to some of the main characteristics found on basaltic (low viscosity) lava flows and traditionally used to categorise them. In particular, they include submarine 'pillow basalts', submarine jumbled plates, sub-aerial ropy pahoehoe and sheet pahoehoe flows where "pahoehoe" refers to a smooth glassy surface.

Experiments similar to the wax studies above but using instead a kaolin-PEG slurry [21], which has both the freezing temperature of the PEG and a yield strength, reveal a different sequence of morphologies (Fig. 6.11). Hence the rheology of the interior fluid plays a role in controlling the forms of flow and deformation, even though the rate of solidification relative to advection, expressed in  $\Psi_B$ , again determined which of a sequence of morphologies occurred. At  $\Psi_B > 15$  (fast extrusion and slow cooling) the slurry spread axisymmetrically almost as if there were no cooling; at  $0.9 < \Psi_B < 15$  there were strong rigid plates over most of the surface and later upward extrusion of ridges with smooth striated sides; at  $0.12 < \Psi_B < 0.9$  the flow commenced as a set of four to six (most often five) radially moving lobes having a weak tendency to spiral. Under rapid cooling or very slow effusion,  $\Psi_B < 0.12$ , the lobes were more like vertical spines and were extruded upward only from the vicinity of the source. In these experiments the transitions between regimes were more gradual than those for the viscous fluid. These morphologies strongly resemble qualitative characteristics of many highly-silicic lava domes [14].

There has been no adequate theoretical description of the above cooling and solidifying flows and the various instabilities that lead to asymmetric spreading and irregular structure. Only a gravitational instability in a density stratified lava dome [16] and the surface buckling instability [11,15] have been analysed. There is good agreement between the wavelengths of observed folds (both on 'ropy pahoehoe' and on the laboratory wax flows) and that predicted for the buckling of layers of differing viscosity or yield strength subjected to a compressive stress [4].

## 6.6 Freezing Flows down a Slope

Experiments with solidifying gravity currents have also shown that the effects of a sloping base are important, leading both to a flow elongation down-slope and to greater channelisation of the flow (Fig. 6.12). The down-slope flow can be channelised by solidified edges in the levee and surface folding regimes [17].

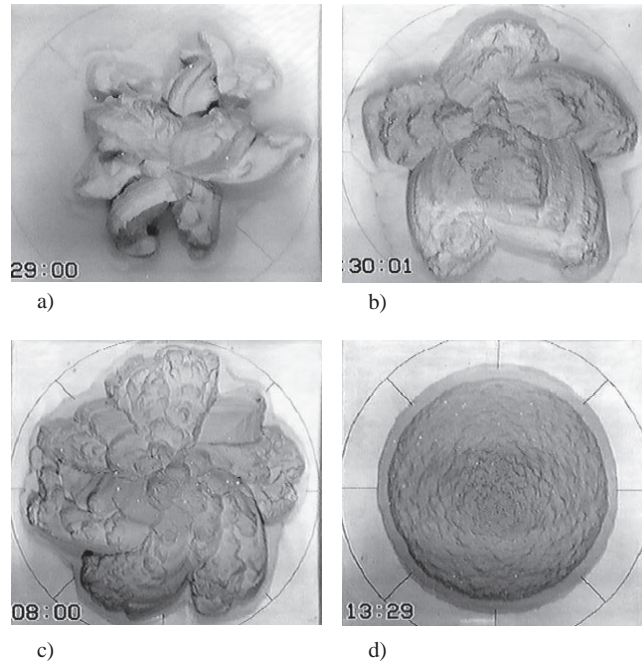


**Fig. 6.11.** Solidifying flows of a Bingham fluid using a slurry of kaolin in PEG. Apart from the fluid rheology the experiments were similar to those of Fig. 8.7. (a) a ‘spiny’ extrusion at  $\Psi_B = 0.09$ ; (b) a lobate extrusion showing a typical 5-lobe pattern at  $\Psi_B = 0.79$ ; (c) a flow without distinct lobes but surfaced by solid plates with curving segments,  $\Psi_B = 1.3$ ; (d) an axisymmetric flow almost unaffected by cooling at  $\Psi_B = 30$ . (Heaviest grid lines are 5 cm apart; from [14])

Hence we have flows that form their own channels, somewhat similar to the large-amplitude flow following fingering in a cooled slot. In contrast to the formation of narrow and fast flow in a small and decreasing number of channels in the cooled slot which implies increasing pressure drop for an imposed volume flux, the free-surface flow can only draw on the gravitational head (the height of the flow) for its forcing. However, in free surface flows there are other mechanisms that allow flow to continue. In particular, the formation of solid crust can lead to covered lava tubes at smaller  $\Psi$  and these tend to increase the insulation of the flow against cooling and thereby further enhance the distance the flow can travel without cooling so much that it solidifies. However, the regimes identified in terms of surface deformation and overall morphology (aside from the down-

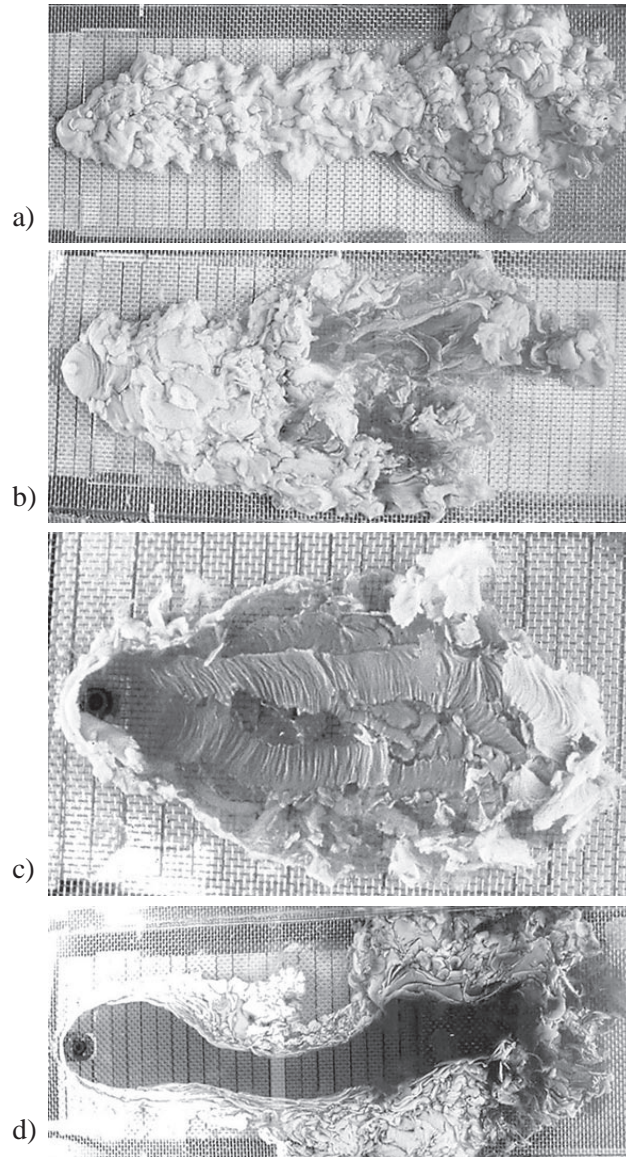


**Fig. 6.12.** Laboratory experiments with PEG wax flowing from a small source on a planar slope under cold water. The base slopes downward to the right and is covered with mesh to make a rough floor. (a) 'pillow' flow; (b) 'rifting' flow; (c) 'folded' flow; (d) 'leveed' flow. (The tank is 30 cm wide; from [17]). (c) and (d) are similar to ropy pahoehoe and long channelised flows observed in Hawaiian lava flows

slope elongation) are not much different from those on a horizontal base, apart from a shift of the regime transitions to smaller values of  $\Psi$  [17].

Turning to observations of long basalt flows that extend for many kilometres from their vent (see e.g. [7]), the flow behaviour again reflects, albeit in ways that remain poorly understood, differing vent fluxes, eruption duration, underlying topography and whether they flow under air or water. Field evidence indicates that surface cooling leads to the formation of a glassy crust while internal mixing in these moderate Reynolds number flows can cause disruption or entrainment of crust, cooling and rheological changes in the interior. The development of levees removes mass from the advancing flow front and represents formation of a flow-defined channel, whereas the solidification of crust to form lava tubes represents a major change in the cooling rate. There are so many processes involved that, in past attempts to model these flows, some processes are approximated by empirical parameterizations. A key factor which has proved particularly difficult to model in a predictive manner is the effect of cooling, which depends on the amount, and rate of disruption, of cooled surface crust. The disruption of crust has been described in terms of a purely empirical parameterisation of the fraction of the surface representing exposed incandescent fluid from the flow interior [10]. Conditions for the disruption and mixing of surface crust under stresses imposed by the underlying flow, and conditions for stable crust, also are not known for either laminar or turbulent flows, yet they determine the distance down-channel at which vertically-mixed flow gives way to stratified flow, the onset of a thickening surface layer [34] and the formation of lava tubes [31,41].

The aim is again to predict factors such as the rate of cooling with distance downstream, flow thickness, the speed of advance of the flow front, changes in flow regime, and the final length of a flow as a function of erupted volume. Given the complexities of long lava flows both simple theoretical results and complex parameterised computational models will be valuable. Significantly, long cooling flows without a prescribed channel have not received much theoretical attention. In this case flow may spread across-slope, form levees or branch (as in numerical experiments with complex distributary systems [36]).

An additional process that can contribute to the pattern of lava flow is melting and thermal erosion of the base underlying a flow. For example, thermal erosion due to melting of underlying sediments or rock by basaltic lava flows was investigated as the cause of sinuous rilles observed on the moon [25,27]. Theoretical modelling [28,29,46] suggests that much hotter and low viscosity melts, called komatiites, which erupted on Earth some 2.7 billion years ago, flowed for large distances as turbulent currents. These would have had high cooling rates under seawater and could have produced thermal erosion 10–100 km from their sources. The extent of melting may have led to significant contamination of the flow by the assimilated melt. Further analysis [50] indicates that erosion is strongly dependent on the nature of the base material, with hydrous sediment being fluidised by vaporised seawater and strongly eroded, whereas relatively little erosion is predicted to occur for consolidated anhydrous sediment.

## 6.7 Conclusions

The dynamics of flows involving cooling and temperature-dependent viscosity, a yield strength, freezing, melting, or dissolution pose many challenges. These flows can form complex shapes and flow patterns, but they can also evolve toward simpler active flow patterns such as a single channel. We have introduced several simplified models which illustrate the nature of some of the underlying flow instabilities. Along with laboratory experiments these models help to explain many characteristics of geological flows. These models also serve as a basis of comparison for more complex models.

Given that magmas in the upper crust and lavas erupted on to the surface have temperatures up to 1200 °C above those of their new environment, but less than only 200 °C above their solidus, it is not surprising that the effects of heat loss can be large. The thermal effects and consequent rheological change (or, in the extreme, solidification) often lead to the onset of a larger viscosity or a yield strength in cooled portions of the flow. This influences the overall flow depth and average spreading rate. In the case of free-surface flows, a yield stress of a surface boundary layer is generally responsible for eventually halting the advance of the flow front. The thermal effects and rheological heterogeneity also lead to a range of complexity and instabilities such as flow fingering, lobes, branching, channelisation, and the formation of surface deformation structures such as folds, ‘ropes’, rifts and faults. Laboratory analog experiments have been invaluable in relating these instabilities to flow conditions, especially the rate of cooling relative to the rate of flow, and base slope. However, many processes remain poorly understood and lacking a theoretical description. In the case of free-surface flows, difficulties are introduced by a moving free surface that is also the boundary at which the thermal and rheological changes tend to be strongly concentrated, and where flow instabilities arise. In the case of melting, dissolution or reaction in permeable media, theoretical difficulties are introduced by large changes in the permeability, which feed back strongly to the flow structure.

## References

1. E. Aharonov, J.A. Whitehead, P.B. Kelemen, M. Spiegelman: *J. Geophys. Res.* **100**, 20,433 (1995)
2. E. Aharonov, M. Spiegelman, P.B. Kelemen: *J. Geophys. Res.* **102** 14, 821 (1997)
3. N.J. Balmforth, A.S. Burbidge, R.V. Craster, J. Salzig, A. Shen: *J. Fluid Mech.* **403**, 37 (2000)
4. M.A. Biot: *Bull. Geol. Soc. Am.* **72**, 1595 (1961)
5. S. Blake: ‘Emplacement Mechanisms and Hazard Implications’. In: *Lava Flows and Domes*, ed. by J.H. Fink (IAVCEI Proc. in Volcanology, vol. 2, 1990) pp. 88–128
6. P.M. Bruce, H.E. Huppert: *Nature* **342**, 665–667 (1989)
7. K.V. Cashman, H. Pinkerton, P.J. Stephenson: *J. Geophys. Res.* **103** 27281–9 (1998)
8. P. Coussot, S. Proust: *J. Geophys. Res.* **101**, 25217 (1996)

9. P. Coussot, S. Proust, C. Ancey: *J. Non-Newtonian Fluid Mech.* **66**, 55 (1996)
10. J. Crisp, S. Baloga: *J. Geophys. Res.* **95**, 1255 (1990)
11. J.H. Fink, R.C. Fletcher: *J. Volcanol. Geotherm. Res.* **4**, 151 (1978)
12. J.H. Fink, R.W. Griffiths: *J. Fluid. Mech.* **221**, 485 (1990)
13. J.H. Fink, R.W. Griffiths: *J. Volcanol. Geotherm. Res.* **54**, 19 (1992)
14. J.H. Fink, R.W. Griffiths: *J. Geophys. Res.* **103**, 527 (1998)
15. J.H. Fink: *Geology* **8**, 250 (1980a)
16. J.H. Fink: *Tectonophys.* **66**, 147 (1980b)
17. T.K.P. Gregg, J.H. Fink: *J. Volcanol. Geothermal Res.* **86**, 145 (2000)
18. R.W. Griffiths, J.H. Fink: *J. Geophys. Res.* **97**, 19739 (1992)
19. R.W. Griffiths, J.H. Fink: *J. Geophys. Res.* **97**, 19729 (1992)
20. R.W. Griffiths, J.H. Fink: *J. Fluid Mech.* **252**, 667 (1993)
21. R.W. Griffiths, J.H. Fink: *J. Fluid Mech.* **347**, 13 (1997)
22. R.W. Griffiths: *Ann. Rev. Fluid Mech.* **32**, 477 (2000)
23. K. Helfrich: *J. Fluid Mech.* **305**, 219 (1995)
24. C.J. Hughes: *Igneous Petrology* (Elsevier Scientific Publishing Company, New York 1982)
25. G. Hulme: *Mod. Geol.* **4**, 107 (1973)
26. G. Hulme: *Geophys. J. Roy. Astr. Soc.* **39**, 361 (1974)
27. G. Hulme: *Geophys. Surv.* **5**, 245 (1982)
28. H.E. Huppert, R.S.J. Sparks, J.S. Turner, N.T. Arndt: *Nature* **309**, 19 (1984)
29. H.E. Huppert, R.S.J. Sparks: *J. Petrol.* **26**, 694 (1985)
30. H.E. Huppert: *J. Fluid Mech.* **121**, 43 (1982)
31. J.P. Kauahikaua, K.V. Cashman, T.N. Mattox, K. Hon, C.C. Heliker, M.T. Mangan, C.R. Thornber: *J. Geophys. Res.* **103**, 27303 (1998)
32. P.B. Kelemen, J.A. Whitehead, E. Aharonov, K. Jordahl: *J. Geophys. Res.* **100**, 475 (1995)
33. P.B. Kelemen, E. Aharonov: 'Periodic formation of magma fractures and generation of layered gabbros in the lower crust beneath ocean spreading centres.' In: *Faulting and Magmatism at Mid-Ocean Ridges*, ed. by W.R. Buck, P.T. Delaney, J.A. Karson, Y. Lagabrielle (Geophysical Monograph 106, American Geophysical Union, Washington DC 1998) pp. 267–280
34. C.R.J. Kilburn: 'Lava crust 'a'a flow lengthening and the pahoehoe-'a'a transition', ed. by C.R.J. Kilburn. In: *Active Lavas* (UCL Press, London 1993) pp. 263–280
35. J.R. Lister: *J. Fluid Mech.* **242**, 631 (1993)
36. H. Miyamoto, S. Sasaki: *J. Geophys. Res.* **103**, 27489 (1998)
37. J.F. Nye: *J. Glaciol.* **2**, 82 (1952)
38. P. Ortoleva, E. Merino, C. Moore, J. Chadam: *American Journal of Science* **287**, 979 (1987)
39. P. Ortoleva, J. Chadam, E. Merino, A. Sen: *American Journal of Science* **287**, 1008 (1987)
40. D.I. Osmond, R.W. Griffiths: *J. Fluid Mech.* (in press 2001)
41. D.W. Peterson, R.T. Holcomb, R.I. Tilling, R.L. Christiansen: *Bull. Volcanol.* **56**, 343 (1994)
42. H. Pinkerton: *Endeavour* **11**, 73 (1987)
43. P.G. Saffman, G.I. Taylor: *Proc. Roy. Soc. A* **245**, 312 (1958)
44. A.H.P. Skelland: *Non-Newtonian flow and heat transfer* (Wiley, New York 1967)
45. M. Spiegelman, P.B. Kelemen, E. Aharonov: *J. Geophys. Res.* (submitted 2000)
46. J.S. Turner, H.E. Huppert, R.S.J. Sparks: *J. Petrol.* **27**, 397 (1986)

47. G.P.L. Walker: *Phil. Trans. R. Soc. A* **274**, 107 (1952)
48. J.A. Whitehead, K.R. Helfrich: *G. Geophys. Res. B3* **96**, 4145 (1991)
49. J.A. Whitehead, P. Kelemen: 'Fluid and thermal dissolution instabilities in magmatic systems'. In: *Magmatic Systems*, ed. by M.P. Ryan (Academic Press, New York, 1994) pp. 355-379
50. D.A. Williams, R.C. Kerr, C.M. Lesher: *J. Geophys. Res.* **103**, 27533 (1998)
51. J. Wylie, J.R. Lister: *J. Fluid Mech.* **305**, 329 (1995)
52. J. Wylie, K.R. Helfrich, B. Dade, J.R. Lister, J.F. Salzig: *Bull. Volcanol.* **60**, 432 (1999)